Journal of MATERIALS RESEARCH

Article
DOI:10.1557/s43578-021-00269-4

MULTISCALE MATERIALS MODELING OF INTERFACE-MEDIATED THERMOMECHANICAL BEHAVIOR

FOCUS ISSUE

A combined experimental and computational analysis on how material interface mediates plastic flow in amorphous/crystalline composites

Amir Abdelmawla[1], Thanh Phan[1], Liming Xiong[1,a)], Ashraf Bastawros[1,a)]

[1] Department of Aerospace Engineering, Iowa State University, Ames, IA 50011, USA
[a)] Address all correspondence to these authors. e-mails: lmxiong@iastate.edu; bastaw@iastate.edu

Received: 29 January 2021; accepted: 5 June 2021; published online: 16 June 2021

Liming Xiong was an editor of this journal during the review and decision stage. For the JMR policy on review and publication of manuscripts authored by editors, please refer to http://www.mrs.org/editor-manuscripts/.

In this work, we study the deformation behavior in amorphous/crystalline metallic composites (A/C-MCs) through nanoindentation experiments and molecular dynamic (MD) simulations. The atomic deformation processes in both crystalline (C-) and amorphous (A-) phases near the amorphous-crystalline interface (ACI) are investigated and correlated with the material's overall constitutive behavior at the microscale. Our major findings are (i) the ACIs enable a co-deformation of the A- and C-phases through "stiffening" the soft phases but "softening" the stiff phases in A/C-MCs through different micro-mechanisms; (ii) there exists an ACI-induced transition zone with a thickness of ~ 10 nm; (iii) the strong coupling between shear transformation zones (STZs) and dislocations can be quantified through carefully designed indentation experiments and simulations; and (iv) the nanoscale MD-simulation-predicted mechanisms can be mapped to the "pop-in" or "excursion" events on the force–indentation depth curves extracted from microscale experiments, although there is a length-scale gap in between.

Introduction

Amorphous alloys, which are formed by rapid quenching to prevent crystallization [1–3], demonstrate limitless desirable properties such as high strength, high elastic properties, and corrosion resistance [4]. However, fast quench rates produce extremely brittle structures, limiting the practical use of such materials [5–9]. To tackle this issue, amorphous and crystalline metals can be integrated into one material system and leads to an amorphous/crystalline metallic composite (A/C-MC). The A/C-MCs combine the advantages of both crystalline (C-) and amorphous (A-) phases [5, 10] to expand the strength–ductility trade-offs by facilitating co-deformations near the amorphous-crystalline interfaces (ACIs), resulting in a significant improvement in strength and ductility [11, 12]. Understanding the effect of ACIs on the overall performance of such composite systems under different loading conditions has attracted great attention recently [13–19]. Nevertheless, the mechanisms responsible for the co-deformation of the A- and C-phases at the ACI remain not fully clear due to two main complexities: (a) there exists a structure transition from atomic-scale short-range order (SRO), to nanoscale medium-range order (MRO), and then to long-range microscale order (LRO) across the ACI; and (b) when such materials are under deformation, especially plastic deformation, the two different plasticity carries, dislocations in C-phases and shear transformation zones (STZs) in A-phases, are strongly coupled with each other [20]. In detail, the plastic flow near an ACI involves dislocation nucleation induced by the interaction between a shear banding and the ACI, and also STZs activation due to an interaction between dislocation-mediated plastic flow and the ACI [11, 19]. The complex material microstructure near the ACI, together with the dislocation-STZ interplay, necessitates a proper characterization of such material's constitutive response near the ACI for understanding its atomistic-to-microscale deformation behavior.

In the past decades, an analysis of the co-deformation between the amorphous and crystalline phases in A/C-MCs

has been intensively attempted through both experimental [6, 11, 12, 15, 18, 21–24] and computational [13, 14, 19, 25–28] efforts. For instance, in one of the most pioneering works, at the macroscale, Wang et al. [11] performed tensile tests on a typical A/C-MC, the multilayered Cu/CuZr nanolaminate, and found that it exhibits a combination of high strength and high ductility. These two properties usually contradict each other in traditional engineering materials. Wang et al. [11] attributed such a unique material property to the presence of the ACIs in Cu/CuZr. In details, they articulated that the ACIs act as the high-capacity sinks for the dislocations, i.e., the ACIs absorb the free volumes and energies carried by dislocations when plasticity flows from Cu to CuZr, although a direct experimental evidence to support this articulation is not provided in their work [11]. This leads to a series of nanoscale experimental studies of the interaction between dislocations and the ACIs in multilayered Cu/CuZr using high-resolution transmission electron microscopy (HRTEM) [22–24, 29]. Near the slip-ACI intersection in multilayered Cu/CuZr nanopillars under compression, it was found [22–24, 29] that the dislocations flowing from Cu to CuZr are not only absorbed by the ACIs as proposed in [11] but also induce a local crystallization, i.e., deformation-induced devitrification (DID) of A-phases at the nanoscale. Zhang et al. [22–24, 29] argued that such DID processes nearby the ACI significantly contribute to the overall performance of A/C-MCs and may "self-toughen" the material during deformation. By contrast, Guo et al. [18] were aware that, when correlating such nanoscale deformation mechanisms with the micro-/macroscale deformation behavior, the characteristic length scales of the material's microstructure, e.g., the layer thickness in multilayered Cu/CuZr, might also play an important role and need to be considered. Their experiments showed that in multilayered A/C-MCs under nanoindentation, the sharp propagation of shear bands near the ACI could only be suppressed when the thickness of the Cu layer was increased from 10 nm to 100 nm. There is no doubt that all the above experiments have largely advanced the understanding of the deformation behavior of A/C-MCs. Nevertheless, the commonly agreed knowledge on the mechanisms responsible for the co-deformations of the A- and C-phases in A/C-MCs is still not established yet due to the lack of answers to a series of questions, such as (i) how does the ACI transfer the plastic flow from C- to A-phases and from A- to C-phases? (ii) is there a transition zone near the ACI? If such a transition zone does exist, at what length scale does it span? Nanometers, micrometers, or even above? Is it possible to control the plastic flow through a fine tune of the characteristic length scale, e.g., the layer thickness of C- and A-phases, of the material's microstructure? (iii) how does such an ACI-induced transition zone affect the activities of dislocations or STZs? Answering these questions at a fundamental level necessitates computer simulations as support for interpreting experimental observations.

Historically, the continuum-level computer simulations based on the theory of plasticity at the macroscopic level have enjoyed the most popularity in understanding how materials plastically deform. Traditional continuum theories are concerned with the macroscopic phenomena in which the smallest characteristic length is much larger than plasticity carriers such as dislocations or STZs. Therefore, a continuum model has a limited resolution and requires empirical constitutive rules for dislocation-/STZ-mediated plasticity and its interaction with the ACIs in A/C-MCs. For example, in a diffuse-interface model [30] for A/C-MCs, the material points in A-phases and C-phases are incorporated with localized slip events. In a recent phase-field model [31] of A/C-MCs, the localized plastic flow is treated as the collective behaviors of structural transformation. The model parameters for either localized slip events or collective behavior of structural transformations need to be pre-determined from experiments or fine scale, e.g., atomistic simulations. With the advent of high-performance computing, molecular dynamics (MD) has become a very powerful tool to study plasticity in crystalline as well as amorphous materials. MD simulations are not only capable of revealing mechanisms but also have the power to link interface structural details with interface properties, as well as to isolate the contributing factors, both of which are difficult to achieve in laboratory-scale experiments. Over the past decades, as far as the deformation behavior of A/C-MC is concerned, extensive MD simulations [13, 14, 19, 25–27] have been performed to gain knowledge that cannot be directly accessible to experiments. For instance, through MD simulation of Cu/$Cu_{46}Zr_{54}$ nanolaminates under uniaxial compression, Arman et al. [19] showed that dislocation-mediated plastic slip in Cu, rather than the loading direction, dictated the orientation of the shear bands (SBs) in CuZr. This is different from traditional wisdom in that the orientation of SBs in amorphous phases is only determined by loading directions. In order to quantify the effect of the characteristic length scale, e.g., the thickness of C- and A-phases, on the constitutive response of A/C-MCs, Jian et al. [25] conducted an MD simulation of plastic deformation of Cu/$Cu_{64}Zr_{36}$ under nanoindentation. One of their major findings is as follows: when the layer thickness was increased from several nanometers to tens of nanometers, there indeed exists a transition from inhomogeneous deformation to co-deformation of C- and A-phases. Obviously, MD simulations are capable of providing valuable information on advancing the understanding of the deformation behavior of A/C-MCs in experiments. However, it should also be fully aware that, due to a large length-scale gap between atomistic simulations and experiments, MD does not resolve all the aspects associated with the complexity of the A/C-MC's deformation behavior yet. Great caution needs to be taken in experimental/computational model setup to achieve a reasonably good correspondence in between.

Otherwise, a direct interpretation of the experimental observations using MD results might be misleading.

As a preliminary attempt along this direction, through leverage of the strengths of MD and nanoindentation experiments, here we perform a series of experimental and computational analysis on how the ACI mediates the plastic flow in A/C-MCs with a primary focus on (a) mapping the atomistic deformation mechanisms to the material's constitutive response, i.e., the force-indentation depth curves, near the ACI under indentation; and (b) quantifying the correlation between indentation depth, dislocation density, and the critical stresses required for dislocation/STZ nucleation near the ACI. This paper is organized as follows. In "Sample preparation, experimental, and computational setup" section, the experimental sample preparation, the nanoindentation setup, the MD computer model, as well as the computational setup (sample preparations, interatomic force fields, boundary conditions, loading conditions, and so on) are introduced. Results from both experiments and MD, such as the force–indentation depth curves, the atomic structure evolution, and the measurement of the critical stress required for dislocation nucleation near the ACI, as well as their dependence on the distance away from the ACI, are discussed and analyzed in "Experimental and simulation results" section. In "Summary and discussion" section, the major findings, limitations of this work, as well as our future research are briefly summarized and discussed.

Sample preparation, experimental, and computational setup

In our experiments, an A/C-MC (Cu/$Ni_{59}Zr_{20}Ti_{16}Si_2Sn_3$) sample is used to study the role of the ACI in the material's response to the nanoindentation. This composite sample is fabricated by the warm extrusion technique [32]. The crystalline phase has an average grain size of 5.8 μm. Before the indentation, the sample is polished to remove any contamination and/or oxidation on the surface. Hysitron TI-950 TriboIndenter and a nanoDMA III transducer with a 90° cube-corner diamond indenter tip with a tip nose radius of 300 nm are used to perform all nanoindentation tests. All indentations are performed under load control mode with a constant strain rate continuous stiffness measurement load function (CMX) with a 500 μN peak load at room temperature. The load profile has three segments. The first segment is performed at a constant loading rate of 16.67 μN/s, while a small oscillatory force is simultaneously superimposed to facilitate continuous measurement of the material response. Thereafter, in the second segment, the indenter is held at the peak load for 2 s before the unloading stage, which lasts for 5 s. We performed 15 indentation sets with 10 (on average) indents across the ACI at shallow angles to increase the spatial sampling resolution across the ACI as well as to obtain a statistically significant dataset. To avoid possible interference of plastic zones of two consecutive indentations, the distance between indents is kept fixed at ~ 2.5 μm. To make sure this separation distance is sufficient, we measured the size of the plastic zone for several impressions according to the empirical relation proposed by [33]. Durst et al. [33] postulated that the radius of the plastic zone, R_{PZ}, can be related to the contact radius, a_c, through a scaling factor, f, such that $R_{PZ} = fa_c$. Here, the plastic zone size factor, f, gives the average contribution of geometric necessary dislocations (GNDs) to the hardness increase at small depths, which is take to be 2.0 for the spherical tip [33]. The estimated plastic zone sizes were much smaller than the gap between adjacent impressions. To eliminate the spatial bias during the indentations, we eliminate results of any wavy ACIs, retaining only data of planner interface, which amounted to more than 95% of all indentation testes. After all indentations are performed, the data are collected and averaged according to their spatial distance from the interface within the A- or C-phase, and thereby suppressing the measurement uncertainties.

In our MD simulations, due to the lack of a well-established interatomic potential for multi-component alloys and, in particular, for the $Ni_{59}Zr_{20}Ti_{16}Si_2Sn_3$ system indented in our experiments, we model the $Ni_{60}Zr_{20}Ti_{20}$ amorphous system to approach the chemical composition of our experimental samples as close as possible. The interactions between species in the $Ni_{60}Zr_{20}Ti_{20}$ are modeled by the embedded atom method (EAM) potential from [34]. In addition, we used a different amorphous system of $Cu_{64}Zr_{36}$ as another reference material to test our hypothesis about the effect of the ACI on the mechanical response of A/C-MCs. The adaptation of the $Cu_{64}Zr_{36}$ model is attributed to several reasons: (i) the CuZr-based A/C-MCs exhibit a combination of high-strength and high-ductility [11], which renders such alloy for potential structural and engineering applications; (ii) several interatomic potentials for this system have been derived and well developed [35–37], which can be directly deployed in our MD simulations without introducing additional uncertainties; and (iii) our previous atomistic models and results in [14] can be leveraged without duplicated efforts. Both $Ni_{60}Zr_{20}Ti_{20}$ and $Cu_{64}Zr_{36}$ amorphous models are generated from a reference FCC single crystal of Ni and Cu atomic arrangements, with the proper concentration of each element such that a small cubic cell of 40 Å side length is constructed for each model. Thereafter, the constructed cells are heated up from 0 K to a temperature of 2000 K, relaxed for 500 ps at 2000 K, quenched from the melting to a temperature below the glass transition temperature, T_g, and relaxed for 500 ps. The cells are then annealed at sub-T_g (T_g is the glass transition temperature) for 600 ns before cooling them down to 300 K from the sub-T_g temperature. All the quenching and equilibration processes are performed under isothermal-isobaric (NPT) ensemble with zero external stress and periodic boundary conditions in all directions, as implemented in LAMMPS [38]. More details on the preparation

of the glassy model have been reported in [14]. Large cells are then obtained by replicating the prepared model along x-, y-, and z-directions. In this way, the replicated cell contains 5.86×10^5 atoms. Thereafter, the replicated cells are annealed at temperatures below T_g to remove any residual stresses [14]. For the $Ni_{60}Zr_{20}Ti_{20}$ sample, the annealing temperature is 850 K ($T_g = 900$ K). In contrast, for the $Cu_{64}Zr_{36}$ sample, the annealing temperature is 700 K ($T_g = 750$ K). The annealed cells are then combined with single-crystal Cu cells with a desired crystallographic orientation, as illustrated in Fig. 2a. Thereafter, the combined samples of Cu/$Cu_{64}Zr_{36}$ and Cu/$Ni_{60}Zr_{20}Ti_{20}$ are equilibrated for another 100 ps. The final computational cell is in a dimension of $25 \times 50 \times 13$ nm^3 and contains 1.3×10^6 atoms. All simulations are conducted using LAMMPs [38] under NVT canonical ensemble at a temperature of 300 K. Periodic boundary conditions along x- and y-directions and traction-free boundary condition along z-direction (indentation), as shown in Fig. 2a. The crystallographic orientation of the C-phase is also shown. To prevent the rigid-body motion of the whole sample in space, five atomic layers at the bottom of the sample ($z = 0$) are fixed. An EAM interatomic potentials [34, 37] and a time step of 2 fs are employed in the simulations. To simulate the material's response to the indentation loading near the ACI, a rigid spherical indenter with a radius of 50 Å is used to indent the model along the vertical direction. During the indentation, the per-atom force induced by the indenter is expressed as follows:

$$F(r) = \begin{cases} -K(r-R)^2, & r < R \\ 0, & r \geq R \end{cases}, \qquad (1)$$

where R is the indenter radius, r is the distance between the atom and the center of the indenter, and K is a force constant, which is set to be 10 eV/Å^2.

Several indentation simulations are performed on each model, with the indentation sites being at different distances away from the ACI. The load–displacement (F–h) curves are directly extracted from the simulations. The OVITO software [39] has been utilized to perform post-processing and to produce snapshots showing the atomic arrangements, the evolution of dislocation structures, as well as the activities of STZs.

Experimental and simulation results

The load–displacement curves

In this section, the load–displacement (F–h) curves extracted from the nanoindentation experiments and MD simulations are presented. In experiments, to assess the effect of the ACI, we performed several sets of indentations (the yellow-dotted line in Fig. 1a) under continuous stiffness measurements mode to a maximum load of 500 μN. Each indentation set has a shallow angle with the ACI (white-dashed line in Fig. 1a) to increase the spatial resolution of sampling the interface region [40] without overlapping each other. The indentation sets start in the amorphous glass region and cross the ACI to the crystalline phase, as shown in Fig. 1a. Several indents are also performed in the amorphous and crystalline phases (blue and green-circled regions in Fig. 1a) to compare the response of each phase close

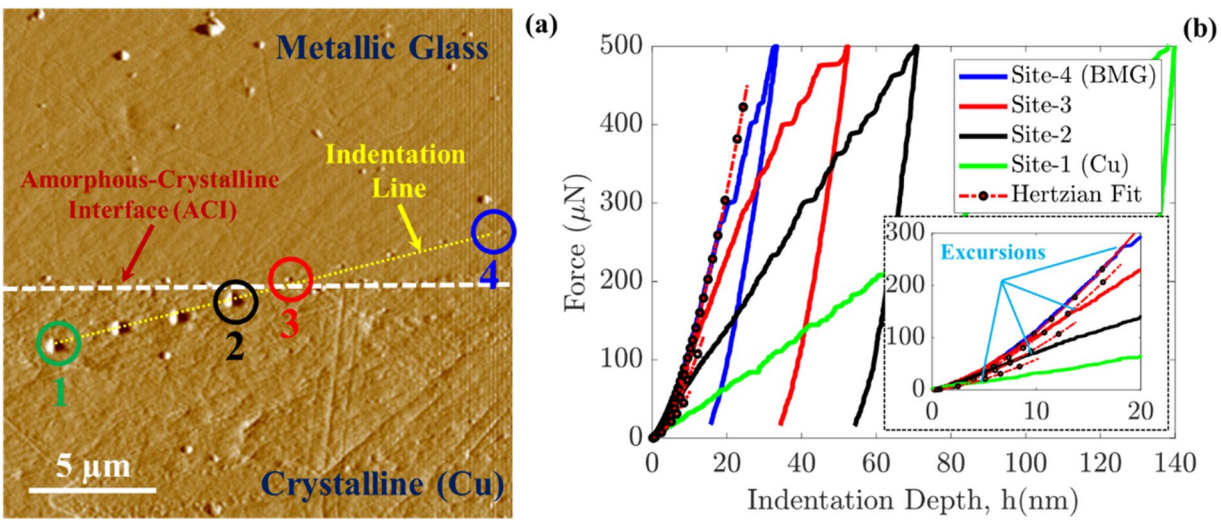

Figure 1: Nanoindentation experiments on a sample A/C-MC system: (a) an illustration for the amorphous/crystalline interface (ACI) and the indentation sites on the sample. Two indentations (black and red circles) are located nearby the ACI (white-dashed line) such that the black circle denotes the indentation nearby the ACI from the crystalline region, whereas the red circle indicates the indentation site nearby the ACI from the amorphous phase. Two indentations (green and blue circles) are located far from the ACI such that the green circle denotes the indentation on the crystalline region and the blue circle represents the indentation site on the amorphous phase; (b) the corresponding force–indentation depth curves for the four selected indentation sites along with the elastic Hertzian fit (red-dashed lines with black circles). The inset in (b) is a magnified view for the elastic portion of the load–displacement curves where the deviation from the Hertzian contact fit can be clearly indicated at the first "pop-in" events.

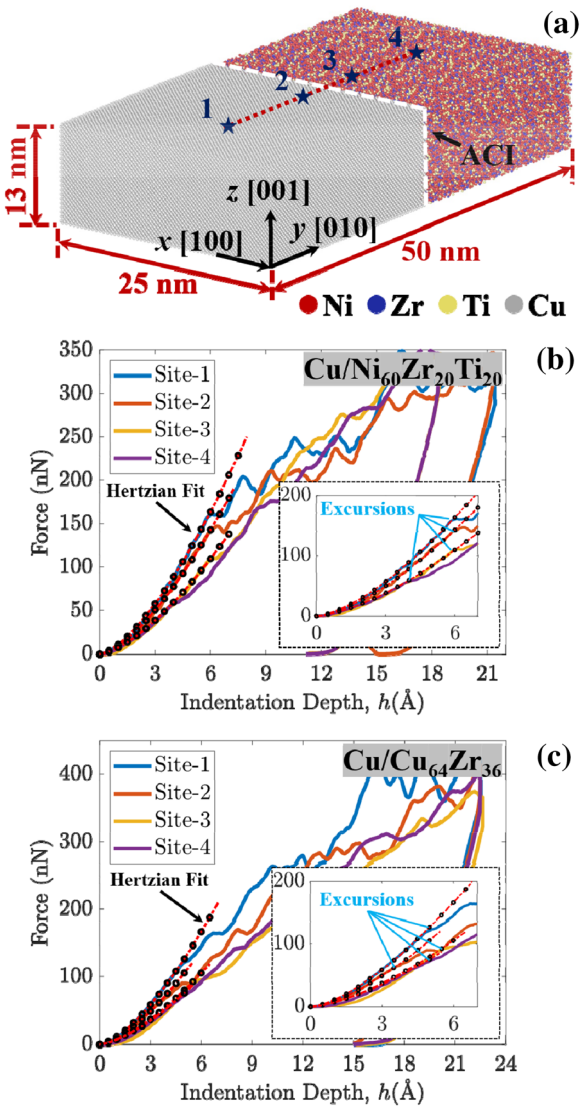

Figure 2: MD simulation of the deformation in $Cu/Ni_{60}Zr_{20}Ti_{20}$ under indentation at a series of different sites: (a) the computer model setup. The gray atoms stand for the crystalline phase (single-crystal Cu), and the red, blue, and yellow atoms refer to Ni, Zr, and Ti species, respectively, in the amorphous phase. Nineteen indentations were performed on the crystalline and amorphous phases at different distances from the ACI (white-dashed line); Two indentations (2 and 3) are located at 20 Å from the ACI in the crystalline and amorphous phase, respectively. Two indentations (1 and 4) are located at 80 Å from the ACI in the crystalline and amorphous phase, respectively; (b) the corresponding force–indentation depth curves for the four selected indentation sites along with the elastic Hertzian fit (red-dashed lines with black circles); (c) the corresponding force–indentation depth curves for the four selected indentation sites along with the elastic Hertzian fit for the $Cu/Cu_{64}Zr_{36}$ sample. The inset in (b) and (c) is magnified views for the elastic portion of the load–displacement curves where the deviation from the Hertzian contact fit can be clearly indicated at the first "pop-in" events.

and far from the ACI on the same grain for the case of the Cu phase. Four corresponding F–h curves for the indentations at sites 1–4 are plotted in Fig. 1b.

In Fig. 1a, site-1 indicates an indentation site in the crystalline phase (Cu) (green circle), site-2 indicates an indentation site at the ACI near the crystalline region (black circle), site-3 is an indentation site at the ACI on the side of the amorphous phase (red circle), and site-4 indicates an indentation site far away from the ACI in the amorphous region (blue circle).

Corresponding to the shift of the indentation sites from site-1, to site-2, to site-3, and then to site-4 (Fig. 1a), the local material's constitutive responses underneath these four different sites significantly differ from each other, as shown in Fig. 1b. Our several major findings are as follows: (i) when the material is indented at sites far away from the material interface ($d/R > 10$), where d is the distance from the indentation site to the ACI, the effect of the ACI on the material's constitutive response is considered to be minor. A comparison of the green curve (site-1, micrometers away from the ACI, an indentation on the Cu side) and the blue curve (site-4, also micrometers away from the ACI, but indentation on the BMG side) in Fig. 1b shows that the amorphous phase, i.e., $Ni_{59}Zr_{20}Ti_{16}Si_2Sn_3$, in this sample is significantly stiffer than the crystalline Cu. Quantitatively, from the blue and green curves in Fig. 1b, the modulus of the amorphous and crystalline Cu phases are estimated from nanoindentation away from the interface to be 139 ± 5.6 GPa and 104 ± 5 GPa, respectively. Here, modulus values are the average values of the steady-state portion of the modulus–indentation depth curves obtained from the continuous measurements during the indentation process. One standard deviation is also noted. This is not surprising because the modulus of a bulk $Ni_{59}Zr_{20}Ti_{16}Si_2Sn_3$ is indeed larger than that of crystalline Cu; (ii) when the material is indented at sites very close to the interface ($d/R < 1$), the presence of ACI may largely alter the material's constitutive response. For instance, the Cu very close to the ACI can be much stiffer than the Cu far away from the ACI. This can be concluded by comparing the black curve (measured from indentation experiments at site-2) with the green curve (measured from indentation experiments at site-1 in Cu phase) in Fig. 1b. Similarly, when comparing the red curve and the blue curve in Fig. 1b, we found that the amorphous phase very close to the ACI is significantly "softer" (site-3, red curve) than its counterpart (site-4, blue curve in amorphous phase) far away from the ACI. Overall at the scale of the experiment, the ACI seems to have "stiffened" the soft phase (Cu here) but "softened" the stiff phase (amorphous phase here) instead. Quantitatively, we also measured the critical force, i.e., the force at the first displacement excursion where the load–displacement curve deviates from the Hertzian fit (indicated by light blue lines in the inset of Fig. 1b). When the indentation site is located on the crystalline Cu side, this critical force might be used to calculate the critical shear stress required to nucleate a homogeneous dislocation loop, τ_{cr}, underneath the indenter (see more details in "The critical stresses, τ_{cr}, and the dislocation density

in the sample under indentation at τ_{cr}" section). When the indentation site shifts from site-1 to site-2 and site-3, the critical force increases from 18 μN at site-1 in the crystalline Cu to 62 μN and 154 μN, respectively. The critical indentation depth, at which the critical force has occurred, also increases as the indenter approaches the ACI. In detail, it increases from 4.7 nm at site-1 to 8.4 nm and 13.9 nm at site-2 and site-3 nearby the ACI, respectively; (iii) there clearly exists a finite-sized transition zone near the ACI, and this transition zone is believed to play an important role in enabling a co-deformation of crystalline and amorphous phases in A/C-MCs.

In order to provide a direct evidence to support that such a transition zone near the ACI does exist, here we also perform MD simulations to investigate the material's constitutive response at a series of indentation sites with different distances away from the ACI. Figure 2a shows our MD model setup for a bi-layered Cu/$Ni_{60}Zr_{20}Ti_{20}$ sample, which is also similar to the Cu/$Cu_{64}Zr_{36}$ sample. Different from many existing MD simulations where an ultrahigh cooling rate at a level of 10^7–10^{13} K/s is used for preparing the amorphous phases in such materials, here, the amorphous phases of $Cu_{64}Zr_{36}$ and $Ni_{60}Zr_{20}Ti_{20}$ are prepared at an experimentally comparable cooling rate of 10^4 K/s as described in detail in Ref. [14]. An indentation loading is imposed at a series of indentation sites (Fig. 2a) with different distances away from the ACI, at a constant indentation velocity of 0.05 (Å/ps) which is equal to 5 (m/s). To investigate the effect of loading rate, we performed indentations at four different indentation velocities ranging from 1 to 20 m/s. Our results reveal that the loading rate has a negligible effect on the elastic responses of the tested sample as well as the location of the first "pop-in" events. However, when the comparison between computer simulations and experiments becomes a purpose, the indentation speed needs to be carefully controlled in MD. Given the micrometer-level sample size and the low indentation speed (16.67 μN/s, which corresponds to an indenter velocity in the range of 1–5 nm/s) in our current nanoindentation experiments, we consider our experimental samples to be deformed in a quasi-static manner. Thus, to approximate such a loading condition, although an indentation speed of 5 m/s has been applied in our MD simulations, the simulation cell is allowed to relax for a duration of 10 ps after each unit increase of the indentation depth to mimic a quasi-static loading strategy. In this way, the simulation cell is considered to be in an equilibrium state during the whole indentation process.

Figure 2b–c shows the force–indentation depth curves extracted from a series of MD simulations of Cu/$Ni_{60}Zr_{20}Ti_{20}$ and Cu/$Cu_{64}Zr_{36}$, respectively, under indentation at a variety of sites on both crystalline and amorphous sides. It is seen that: (i) again, when the indentation site is away from the interface, e.g., 8 nm (site-1) away from the ACI in this nanoscale MD model ($d/R = 1.6$), the effect of the ACI on the material's constitutive response to the indentation loading is negligible. Thus, the force–indentation depth curves extracted from MD simulation at site-1 (blue curve) and site-4 (purple curve) are considered to be for bulk crystalline Cu and either of the glassy phases, respectively. Different from $Ni_{59}Zr_{20}Ti_{16}Si_2Sn_3$ in our experiments where the amorphous phase has a larger modulus than crystalline Cu, here the amorphous $Ni_{60}Zr_{20}Ti_{20}$ phase (purple curve) in our MD models, while stiffer than the $Cu_{64}Zr_{36}$, are obviously less stiff than the crystalline Cu phase (blue curve). This seems to be counter intuitive and may not be consistent with some experimental observations [41–43] but agrees well with the results from many existing MD simulations [13, 44–48], which use the same empirical potentials and cooling rates; (ii) on the side of the stiffer phase (Cu in MD models), when the indentation site gets closer to the ACI, i.e., a shift from site-1 to site-2, and then to site-3 (Fig. 2a) ($d/R < 1$), the slopes, the critical forces as well as the critical depths (indicated by the deviation from Hertzian contact response and/or the 'excursions' in the inset pictures of Fig. 2b–c) on the force–indentation depth curves decrease (Fig. 2b–c). Similarly, on the side of the softer phase ($Ni_{60}Zr_{20}Ti_{20}$ or $Cu_{64}Zr_{36}$ in MD models), the slopes, the critical forces, as well as the critical depths (indicated by the 'excursions' in the inset pictures of Fig. 2b–c) on the force–indentation depth curves, also decreases (yellow and purple curves in Fig. 2b–c) when the indentation site approaches the ACI by shifting from site-4 to site-3. Clearly, this result confirms our experimental finding on "the ACI stiffens the soft phase ($Ni_{60}Zr_{20}Ti_{20}$ or $Cu_{64}Zr_{36}$ in MD models) but softens the stiff phase (Cu in MD)"; (iii) a finite-sized transition zone nearby the ACI can be, thus, also identified from our MD simulations within the range of $-1 < d/R < 1$. Although the transition zone spans a significantly less physical space than that in experiments due to a length-scale mismatch between our current nanoscale MD simulations and microscale indentation experiments, when normalized with the indenter radius, the transition zone spans a similar relative range of d/R ratio for both cases.

The critical stresses, τ_{cr}, and the dislocation density in the sample under indentation at τ_{cr}

In order to quantify the size of the transition zone near the ACI as well as the effect of the ACI on the material's behavior, dislocation nucleation, or STZ activation, for instance, here in our nanoindentation experiments and MD simulations, we measure the critical shear stress, τ_{cr}, together with the corresponding dislocation density,ρ, at each indentation site in the Cu phase. As mentioned before, the critical shear stress, τ_{cr}, which occurs when the force underneath the indenter reaches a critical value corresponding to the first dislocation excursion noted by deviation from the initial Hertzian contact. The corresponding τ_{cr} can be calculated from the elastic Hertzian contact, using Eq. (2) [49–51] as follows:

$$\tau_{cr} \approx 0.31\left(\frac{6E^2}{\pi^3 R^2}F_{cr}\right)^{1/3}, \qquad (2)$$

where E is the reduced modulus (in our experiment $E = 105$ GPa; in our MD simulation $E = 67$ GPa for the C-phase), R is the radius of the indenter (in our experiment $R = 300$nm; in our MD simulations $R = 5$nm), and F_{cr} is the critical force at the deviation from Hertzian contact or first excursion in both experiment and MD.

In MD simulations, the reduced modulus values were calculated based on the linear fitting of the upper one-third of the unloading curves at each indentation site using the Oliver-Pharr method [52]. The modulus value of 67 GPa is for the bulk single-crystal copper (i.e., far from the ACI).

We then assess the dislocation density underneath the indenter in both the experimental setup and the MD simulation as a function of proximity from the ACI. In experiments, we utilize the continuum-level theories [33, 53–55] to relate the macroscopic hardness of the material, H, with the density, ρ, of dislocations underneath the indenter through a Taylor hardening model [55] using von Mises' rule [53] and Tabor's factor of 3 to correlate the hardness and flow stress [33, 54]. First, the hardness is directly measured from the continuous stiffness measurements mode to calculate the actual contact depth. We evaluate the hardness first from F_{cr} and the corresponding contact area, A_c, such that

$$H = \frac{F_{cr}}{A_c} \tag{3}$$

The corresponding dislocation is then calculated from the correlations:

$$\begin{aligned} H \equiv 3\sigma &= 3\sqrt{3}\tau \\ &= 3\sqrt{3}\alpha\mu b\sqrt{\rho} \end{aligned} \tag{4}$$

where σ is the normal flow stress, τ is the shear flow stress, μ is the shear modulus, which is estimated to be 26 GPa for Cu single crystal, α is a constant and taken to be 0.5 in our model [56], b is the magnitude of Burger vector, which is 2.55 Å for Cu (in our calculations), and ρ is the total dislocation density.

Here, the shear modulus is obtained by utilizing the relation between Young's modulus, E, Poisson's ratio, ν, and the shear modulus, μ, such that $\mu = E/2(1+\nu)$. In our study, we use the reported value in the literature of Poisson's ratio of copper of 0.35 [57, 58]. In MD simulations, we use the Dislocation Extraction Algorithm (DXA) embedded in OVITO software [39] to extract the total length of the dislocation underneath the indenter at the critical indentation depth (depth at the critical force). The dislocation density is obtained by dividing the dislocation length by the volume of the cell. Furthermore, we extended the same procedure highlighted by Eqs. (3, 4) to get the projected dislocation density right after nucleation in MD. In detail, we measure the contact area in LAMMPS by checking the in-contact atoms with the indenter at each time step. We then calculate the highest and lowest z coordinates of the in-contact group of atoms. By subtracting the lowest z from the highest z, we obtained the true contact depth, h_c. Thereafter, the area of the spherical cap produced by the indenter is computed at each time step such that $A_c = 2\pi R h_c$. Ultimately, by implementing the hardness values obtained using Eq. (3) into Eq. (4), we can approximately estimate the total density of dislocations involved in the plastic zone underneath the indenter. We found that the obtained dislocation density from the DXA algorithm and that from Eq. (4) was in good agreement.

The critical shear stress, τ_{cr}, required for dislocation nucleation in Cu phases, the inverse of the dislocation density, ρ^{-1}, underneath the indenter at τ_{cr}, as well as the distance, d, between the indentation site and the ACI, are correlated with each other in Fig. 3. In this figure, the data from both experiments and MD simulations have been included. Figure 3 shows that (i) in experiments, τ_{cr} increases with the decrease of distance d from the ACI. This is reasonable because, as discussed before, in a $Cu/Ni_{59}Zr_{20}Ti_{16}Si_2Sn_3$ system, "the ACI has stiffened the soft phase", i.e., Cu, nearby; and (ii) in MD simulations, τ_{cr} decreases with the decrease of d instead. This is also consistent with our previous argument on "the ACI has softened the stiff phase, i.e., Cu, in $Cu/Ni_{60}Zr_{20}Ti_{20}$ and $Cu/Cu_{64}Zr_{36}$ systems." Quantitatively, in experiments, τ_{cr} increases from 2.2 to 3.7 GPa when the indentation site is shifted from $d \approx 5.8$ μm to $d \approx 0.17$ μm or d/R shifted from 14.5 to 0.425. In contrast, in MD simulations of $Cu/Cu_{64}Zr_{36}$, τ_{cr} decreases from 4.8 to 3.3 GPa when the indentation site is shifted from $d \approx 8.0$ nm to $d \approx 0.5$ nm (d/R shifted from 1.6 to 0.1). The dislocation density remains constant far from the ACI for as indicated from the experiment and MD simulations, as shown in Fig. 3. Both experimental and MD simulation results presented here for the same range of d/R ratio, though with different spatial resolution, suggest that, through correlating the critical stress, τ_{cr}, with the distance, d, between the indentation site and the ACI, high-throughput nanoindentation tests may be utilized to assess the thickness of an ACI as well as its quantitative effect on the material's local constitutive behavior. Also, although there exists an agreement between our current experiments and MD simulations, such an agreement is only qualitative at this stage and should be taken with caution. A quantitative agreement between our current simulations and experiments has not been achieved yet due to the limited length scales in MD. This is also one major reason why the critical stress, τ_{cr}, and also the dislocation density, ρ, in our simulations are significantly higher than that in experiments (Fig. 3). Furthermore, it can be noted that the critical shear stress of the Cu phase in the $Cu/Ni_{60}Zr_{20}Ti_{20}$ system (blue crosses in Fig. 3) is slightly higher than the stress of the same phase in the $Cu/Cu_{64}Zr_{36}$ system (red circles in Fig. 3). Such difference is attributed to the difference in the two EAM potentials used in our study [34, 37].

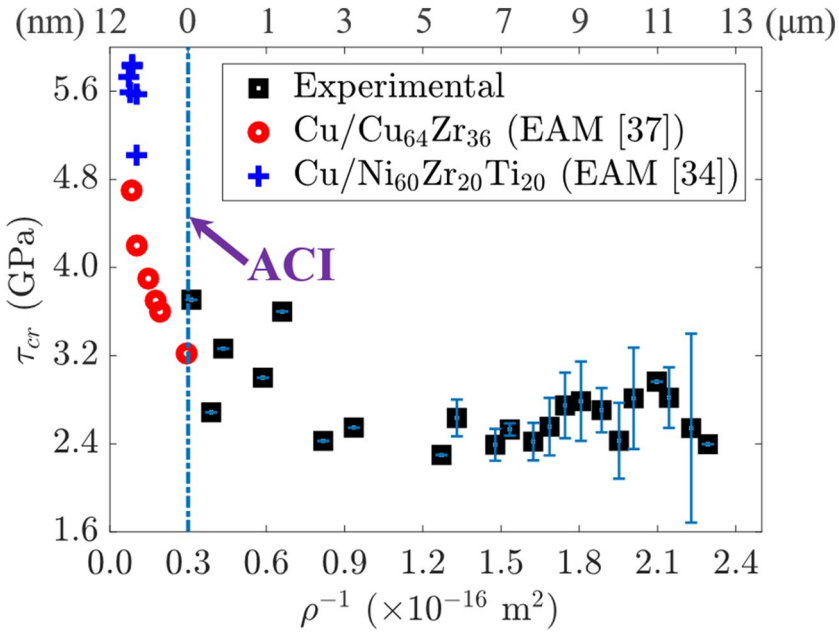

Figure 3: The variation of the critical shear stress with respect to the inverse of the density, ρ, of dislocations underneath the indenter at different distances, d, away from the ACI (top scale; Right experiment in μm, Left MD in nm). The black boxes with error bars in the plot represent the experimental data, and red circles and blue crosses stand for data from MD simulations for $Cu/Cu_{64}Zr_{36}$ and $Cu/Ni_{60}Zr_{20}Ti_{20}$, respectively. Experimental data are averaged, and errors bar with ± 1 standard deviation from the mean superimposed on the data points.

To fill the length-scale gap between MD and experiments, a multiscale computer model, e.g., the recent concurrent atomistic-continuum (CAC) model [59–69] that can simultaneously resolve the long-range dislocation-mediated plasticity and the atomic-level complexities nearby the ACI, is needed and will be discussed in "Summary and discussion" section.

As a preliminary attempt of using the obtained data to quantify the thickness of an ACI, Fig. 4a and b presents the experimental and computational results, respectively, to correlate the critical shear stress, τ_{cr}, with the distance, d, between the indentation site and the ACI. Here, d is normalized by the radius, R, of the indenter to achieve a dimensionless comparison between MD and experiments. Figure 4 shows that, according to the level of critical shear stress, the whole A/C-MC sample can be clearly split into three regions. This includes two bulk regions (crystalline and amorphous), where the ACI serving as a finite-sized transition zone between C- and A-phases can be clearly identified. In this zone, the shear stress distribution has the maximum variance. As we utilized two different interatomic potentials for the $Cu/Cu_{64}Zr_{36}$ [37] and $Cu/Ni_{60}Zr_{20}Ti_{20}$ [34]

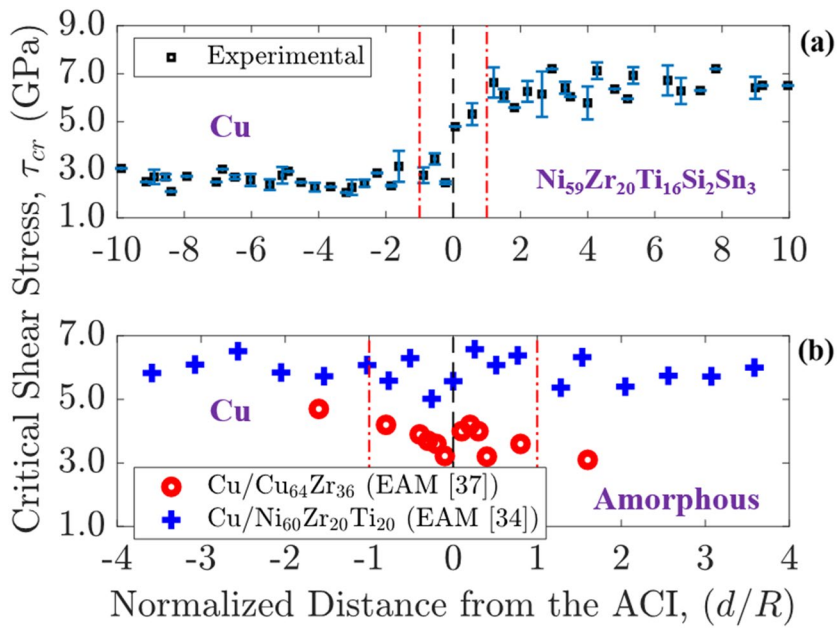

Figure 4: The variation of the critical shear stress, τ_{cr}, as a function of the distance away from the ACI. Here the distance, d, is normalized by the radius, R, of the indenter tip. (a) Acquired trend from experiments. Experimental data are averaged on multiple indentation lines across ACI, with one standard deviation shown. (b) Acquired trend from MD simulations for $Cu/Cu_{64}Zr_{36}$ and $Cu/Ni_{60}Zr_{20}Ti_{20}$, over approximately the same normalized range, though with very different spatial resolutions.

systems, the critical shear stress of the Cu phase in the two systems is slightly different, as shown in the Cu side in Fig. 4b. It is also worth pointing that the modulus of the $Ni_{60}Zr_{20}Ti_{20}$ is higher than $Cu_{64}Zr_{36}$ which leads to an increase in the shear stress, as shown in the amorphous side in Fig. 4b. Based on our MD simulation results, as shown in Fig. 4b, the thickness of this zone can be estimated to be ~ 10 nm. By contrast, in experiments, due to the limited number of data points and limited spatial resolutions, we cannot accurately measure the ACI's thickness yet. However, we may still project an interface thickness from a numerical calibration of the hardness and moduli near the ACI as illustrated in [40], where the thickness of a transition zone near a polymeric interface was measured through nanoindentation tests. Using a scaling law in [40], the experimentally estimated thickness of ACI in Fig. 4a could be in the order of ~ 100 nm, which is an order of magnitude larger than that from the present MD simulations but can be achieved through CAC simulations [59–69]. Though, several critical observations can be highlighted, especially for the $Cu/Cu_{64}Zr_{36}$ system. (i) In the C-phase, a gradual reduction of τ_{cr} can be observed as the indentation site is nearing the ACI for $d/R < 1$. This could be attributed to an ACI-induced stress concentration, which would reduce the dislocation nucleation barrier. Such trend cannot discreetly be observed in the experiment due to the resolution limitations. (ii) In the A-phase, a slight increase in τ_{cr} could be identified within $d/R < 0.5$. This might be attributed to the increase in randomness near the interface and thereby increase the stress level required for nucleation of STZs near the ACI. We have not been able to clearly identify these trends in the experimental measurements due to the lack of measurement resolution and disparity in scales. These trends might also be identified in Fig. 4b for the $Cu/Ni_{60}Zr_{20}Ti_{20}$. However, since both the A- and C- phases have exhibited similar levels of τ_{cr}, a clear trend could not be assertively identified.

Mapping the atomistic mechanisms to the constitutive responses of A/C-MCs

In this part, leveraging the strengths of MD simulations, we attempt to establish a correlation between the atomistic-simulation-predicted mechanisms and the material's constitutive response characterized from our nanoindentation experiments for A/C-MCs. In particular, the atomic process of the dislocation–STZ interaction and its reflections on the force-indentation depth curves is analyzed in great detail. Figure 5a presents the force–indentation depth curve from nanoindentation experiments with the indentation site being located at site-1, as shown in Fig. 1a. There clearly exist several excursions (circled by the dash lines in Fig. 5a) on the force–indentation depth curve. Since the indentation loading is applied on the crystalline Cu side, the first excursion (circled by the black dash line) is believed to be caused by dislocation nucleation underneath the indenter, as shown in Fig. 5c–f. Once dislocations nucleate, with the increase of the indentation depth, they migrate away from the region underneath the indenter, and some eventually arrive at the ACI, as shown in Fig. 5d–g. When the dislocation-mediated plasticity flows into the amorphous phases, STZs may be activated, shown in Fig. 5e–i. Correspondingly, the second excursion (circled by the blue dash line in Fig. 5a) appears.

An argument that the 2nd excursion is for STZ activation and the 1st excursion is for dislocation is based on a clear observation on the force–indentation depth curve: the occurrence of the 2nd excursion spans a significantly larger indentation depth increase than the 1st excursion does. This is reasonable because the activation volume of STZ is significantly larger than that of dislocations. As further evidence to support this interpretation, Fig. 5b-i presents the MD-simulation-predicted force–indentation depth curve, the dislocation structure evolution, and also the STZ activation upon the dislocation's arrival at the ACI, respectively. Similar to what has been observed in Fig. 5a, two excursions (one for dislocation nucleation, the other is for STZ activation) are also seen on the force–indentation depth curve from MD (Fig. 5b). Corresponding to the 1st and the 2nd excursions in Fig. 5b, c–g present the dislocation nucleation underneath the indenter and the structures of dislocations when they start interacting with the amorphous phases. When dislocations are absorbed by the ACI, STZs can be activated, as shown in Fig. 5e–i. The above analysis also suggests that when the C-phase in an A/C-MC is indented, STZs may be activated with the dislocation-mediated plasticity flow from C- to A-phase.

Based on the above result, an immediate hypothesis that we can make is: when the A-phase in an A/C-MC is indented, dislocations may be activated with the STZ-mediated plasticity flow from A- to C-phase. Both nanoindentation experiments and simulations have been performed to test this hypothesis. The relevant results are presented in Fig. 6. In Fig. 6a (experimental results) and Fig. 6b (MD simulation results), when the A-phase is indented, the first notable excursion (black-dashed ellipse in Fig. 6a and b) is believed to be caused by the activation of STZs underneath the indenter. This can be clearly evidenced in the snapshots of the atomic arrangements from MD simulations at an indentation depth of 10 Å (Fig. 6c–e). With the increase of the indentation depth, the second burst occurs on the force–indentation depth curve and is believed to be caused by dislocation nucleation in the A-phase upon the arrival of the STZ-mediated plasticity at the ACI (Fig. 6d–f).

Overall, there obviously exists a good correspondence between our nanoscale MD simulations and microscale indentation experiments, although this correspondence is only qualitative at this stage. In this work, again, due to the length scale and spatial resolution gaps between MD and experiments, a quantitative agreement, indentation forces, and depths in particular,

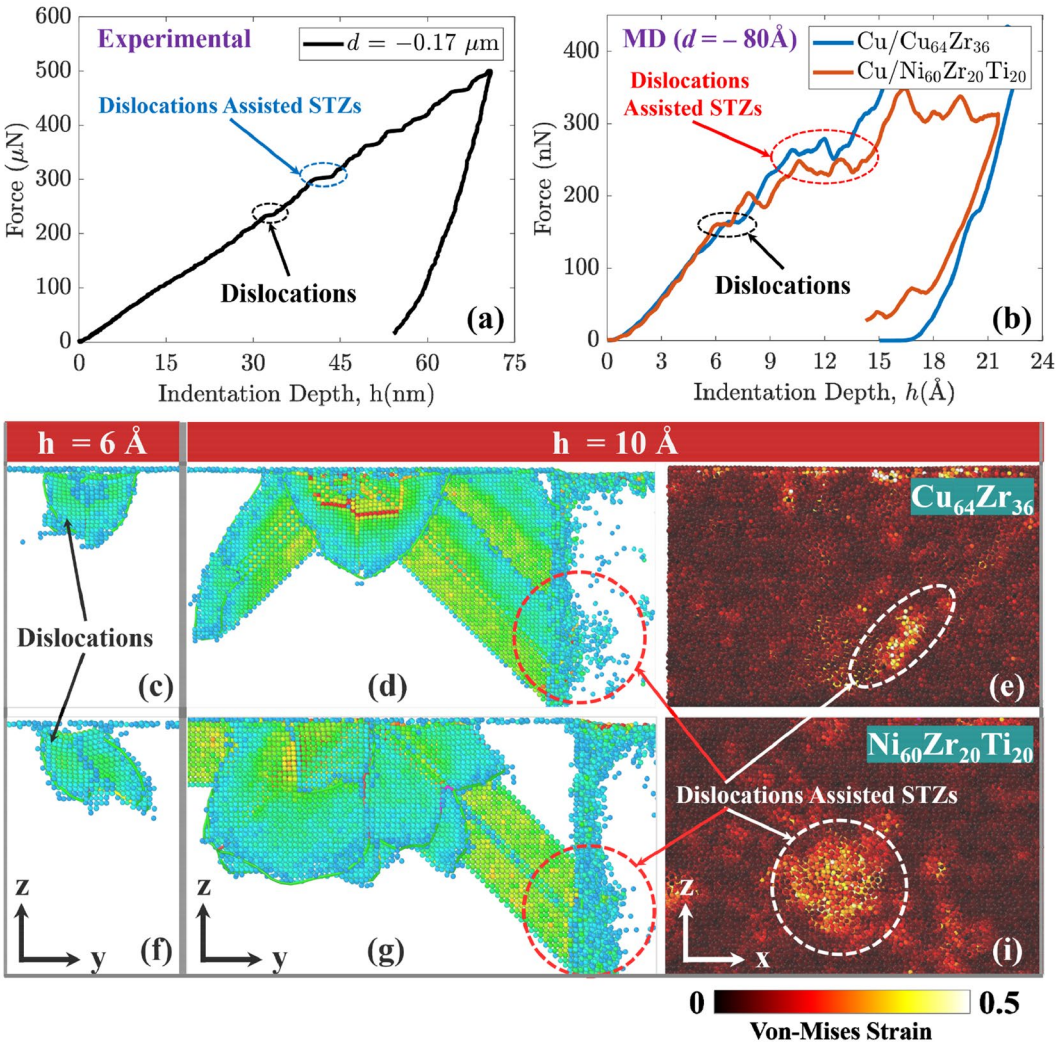

Figure 5: The atomistic-simulation-based mechanism for the dislocation-assisted STZ activation and its connection with the material's constitutive behavior characterized in experiments: (a) the force–indentation depth curve from an indentation experiment on the Cu side at a site of 0.17 μm ($d/R = 0.425$) away from the ACI (the black circle in Fig. 1a); (b) the force–depth curve from molecular dynamics (MD) simulation of indentation on the Cu side at a distance of 8 nm away ($d/R = 1.6$) from the ACI; (c–d) and (f–g) are two sets of snapshots from MD simulations for Cu/$Cu_{64}Zr_{36}$ and Cu/$Ni_{60}Zr_{20}Ti_{20}$, respectively, of dislocation (light blue atoms) and stacking fault (green atoms) structure evolution in Cu underneath the indenter at site-1 with an indentation depth of 6 Å and 10 Å, respectively. Here only the atoms participating in dislocations and stacking faults are displayed through coloring them using the centrosymmetry parameter; and (e and i) the activation of STZs in the $Cu_{64}Zr_{36}$ and $Ni_{60}Zr_{20}Ti_{20}$, respectively, when the dislocations arrive at the ACI. Here, the atoms are encoded with the atomic-level von Mises strain implemented in OVITO. The atoms with a strain of 0.2 and above are considered participating STZs.

between experiments and computer simulations have not been achieved yet but will be intensively pursued in our future work through the deployment of a concurrent atomistic-continuum approach [59–69].

Summary and discussion

In this paper, we present a combined experimental and computational analysis on how the buried material interface mediates the plastic flow in amorphous-crystalline metallic composites under nanoindentation. We have (i) characterized the local constitutive behavior of the materials nearby the ACI through extracting the force–indentation depth curves through both experiments and simulations; (ii) measured the critical stress required for dislocation nucleation when the crystalline phase in A/C-MC is indented at sites nearby the ACI; and (iii) mapped the atomistic-simulation-revealed deformation mechanism to the force–indentation depth curves obtained from indentation experiments. Our several major findings are (1) a co-deformation of the C- and A-phases can be achieved because the ACI "stiffens" the soft phase but "softens" the stiff phase in an A/C-MCs; (2) there

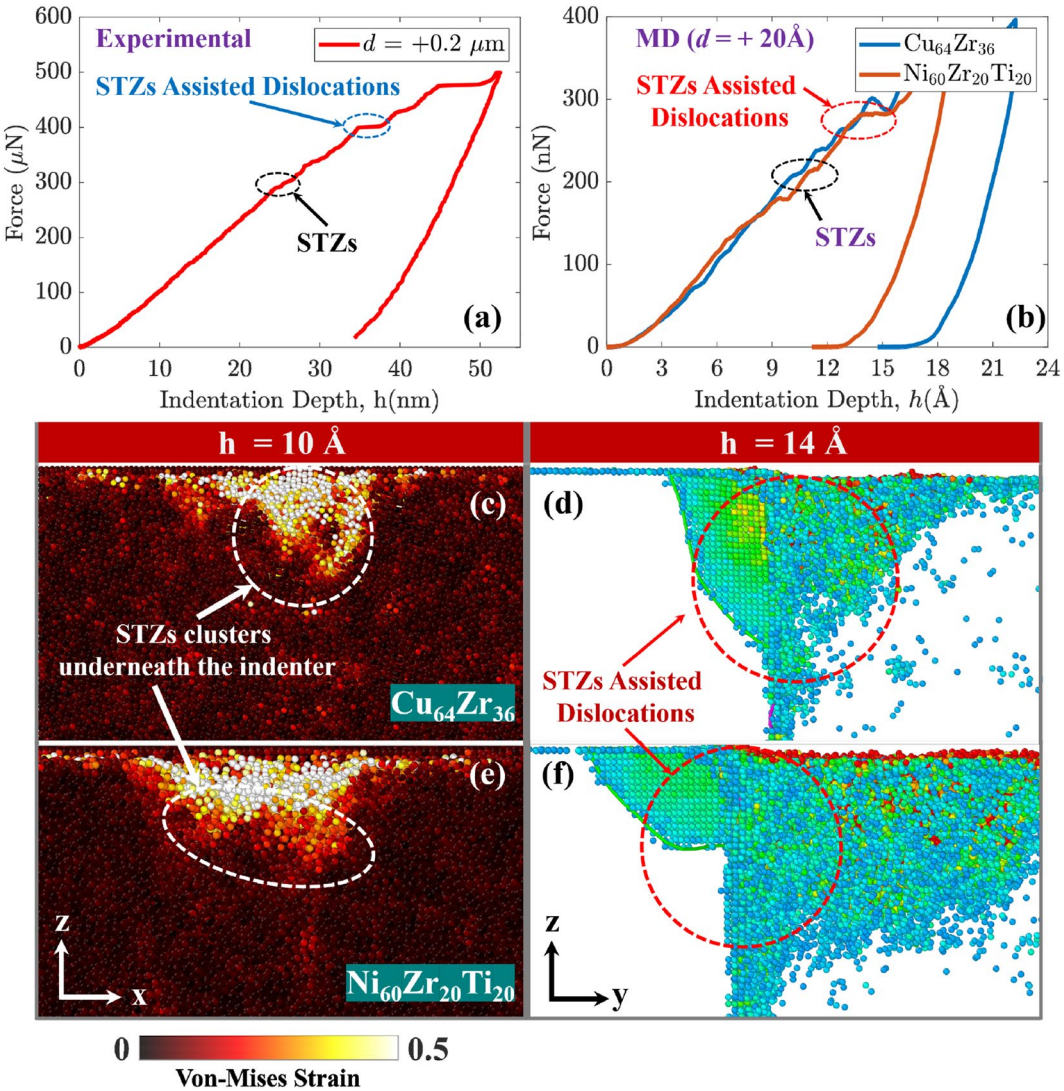

Figure 6: The atomistic-simulation-based mechanism for the STZ-induced dislocation nucleation and its connection with the material's constitutive behavior characterized in experiments: (a) the force–indentation depth curves from an indentation experiment on the $Ni_{59}Zr_{20}Ti_{16}Si_2Sn_3$ side at a site of 0.2 μm away from the ACI (the black circle in Fig. 1a); (b) the force–depth curve from molecular dynamics (MD) simulation of indentation on the amorphous side at a distance of 2 nm away from the ACI; (c-e) one snapshot from MD simulations showing the activation of STZs when the amorphous phase in $Cu/Cu_{64}Zr_{36}$ and $Cu/Ni_{60}Zr_{20}Ti_{20}$, respectively, is under indentation. Here, the atoms are encoded with the atomic-level von Mises strain implemented in OVITO. The atoms with a strain of 0.2 and above are considered participating STZs, and (d–f) the dislocation (light blue atoms) and stacking fault (green atoms) structure evolution in Cu when the STZ-mediated plastic flow arrives at the ACI. Here only the atoms participating in dislocations and stacking faults are displayed through coloring using the centrosymmetry parameter.

exists an ACI-induced transition zone in compromising the properties of C- and A-phases in between. According to our MD simulations, the finite thickness of this transition zone is at a level of ~ 10 nm. This, of course, needs to be further confirmed from high-fidelity experiments and will depend on material chemistry, processing conditions, and many other factors; and (3) when the dislocation-mediated plasticity flows from the C- into the A-phase, STZs can be activated, and vice versa, when the STZ-mediated plasticity flows from the A- into the C-phase, dislocations may be nucleated. Such a two-way coupling between dislocations and STZs has been confirmed by our MD simulations and also reflected on the force–indentation depth curves extracted from experiments.

The knowledge gained from this research may be utilized to advance the understanding of the deformation behavior of A/C-MCs and, in turn, provide support for designing such material systems with an optimized property. However, it should be taken with caution due to several major limitations of this work: (1) the chemistry of the material system in the present experiment ($Cu/Ni_{59}Zr_{20}Ti_{16}Si_2Sn_3$) is different from that in MD simulations in ($Cu/Ni_{60}Zr_{20}Ti_{20}$) and ($Cu/Cu_{64}Zr_{36}$). The material chemistry mismatch may have

introduced uncertainty when comparing experimental results with that from MD. Such uncertainty might be suppressed through (a) performing MD simulations of deformation in $Cu/Ni_{59}Zr_{20}Ti_{16}Si_2Sn_3$ once a reliable interatomic force field is established for such a complex system or (b) fabricating the $Cu/Cu_{64}Zr_{36}$ materials and conducting the corresponding in-house indentation experiments. This is currently being attempted through a collaboration with DOE Ames Laboratory and will be reported in our future work; (2) the length scale (sample size, indenter size, etc.) in the present nanoscale MD model is significantly smaller than that in experiments. The properties obtained by such nanoscale MD obviously do not necessarily reproduce the values in experiments due to its severe spatiotemporal limitations. In particular, the MD model contains only two layers with a layer thickness of ~ 13 nm (in the z-direction). Such atomistic models (a) will not be able to predict the overall performance of A/C-MCs because each ACI in such materials does not exist in isolation and its evolution depends on the surrounding microstructures; (b) will enforce the absence of dislocation arrays and will only allow the confined slip mediated by single dislocations gliding in C-phases. Such MD models alone, thus, can neither model the complex microstructure nor predict its macroscale constitutive responses. Understanding the plastic deformation in A/C-MCs necessitates experimentally validated multiscale simulations to overcome many inherent limitations in continuum and fully atomistic models. This will be attempted and reported through the deployment of our concurrent atomistic-continuum method [59–69].

Acknowledgments

We acknowledge the support of the US National Science Foundation (NSF) with an award number of DMR-1807545 and the Extreme Science and Engineering Discovery Environment (XSEDE-TG-MSS170003 and XSEDE-TG-MSS190008). TP and LX also acknowledge the support of NSF under an award number of CMMI-1930093.

Data availability

The datasets generated during and/or analyzed during the current study are available from the corresponding author on reasonable request.

Declarations

Conflict of interest On behalf of all authors, the corresponding author states that there is no conflict of interest.

References

1. M. Chen, Mechanical behavior of metallic glasses: microscopic understanding of strength and ductility. Annu. Rev. Mater. Res. **38**, 445–469 (2008)
2. J.P. Chu, J.S.C. Jang, J.C. Huang, H.S. Chou, Y. Yang, J.C. Ye et al., Thin film metallic glasses: unique properties and potential applications. Thin Solid Films **520**(16), 5097–5122 (2012)
3. M. Chen, A brief overview of bulk metallic glasses. NPG Asia Mater. **3**(9), 82–90 (2011)
4. J. Schroers, The superplastic forming of bulk metallic glasses. JOM **57**(5), 35–39 (2005)
5. A. Donohue, F. Spaepen, R.G. Hoagland, A. Misra, Suppression of the shear band instability during plastic flow of nanometer-scale confined metallic glasses. Appl. Phys. Lett. **91**(24), (2007)
6. A. Antoniou, A. Bastawros, B. Biner, Experimental observations of deformation behavior of bulk metallic glasses during wedge-like cylindrical indentation. J. Mater. Res. **22**, 514–524 (2007)
7. M.J. Kramer, D.J. Sordelet, A.F. Bastawros, X. Tan, S.B. Biner, Absence of crystallization during cylindrical indentation of a Zr-based metallic glass. J. Non Cryst. Solids **351**, 2159–2165 (2005)
8. A. Antoniou, A.F. Bastawros, C.C.H. Lo, S.B. Biner, Deformation behavior of a zirconium based metallic glass during cylindrical indentation: in situ observations. Mater. Sci. Eng., A **394**, 96–102 (2005)
9. A. Antoniou, S.B. Biner, A.F. Bastawros, Experimental observation of cylindrical indentation of a metallic glass. Materials Research Society Symposium Proceedings, 903, 0903-Z12-0 (2005)
10. A.A. Voevodin, J.S. Zabinski, Load-adaptive crystalline–amorphous nanocomposites. J. Mater. Sci. **33**(2), 319–327 (1998)
11. Y. Wang, J. Li, A.V. Hamza, T.W. Barbee, Ductile crystalline–amorphous nanolaminates. Proc. Natl. Acad. Sci. **104**(27), 11155–11160 (2007)
12. A. Khalajhedayati, Z. Pan, T.J. Rupert, Manipulating the interfacial structure of nanomaterials to achieve a unique combination of strength and ductility. Nat. Commun. **7**(1), 1–8 (2016)
13. D. Zhao, S. Wang, B. Zhu, L. Li, H. Zhao, Anisotropic deformation behaviors of amorphous-crystalline nanolaminates investigated via molecular dynamics simulations. J. Alloys Compd. **787**, 649–657 (2019)
14. T. Phan, J. Rigelesaiyin, Y. Chen, A. Bastawros, L. Xiong, Metallic glass instability induced by the continuous dislocation absorption at an amorphous/crystalline interface. Acta Mater. **189**, 10–24 (2020)
15. M.C. Liu, J.C. Huang, Y.T. Fong, S.P. Ju, X.H. Du, H.J. Pei, T.G. Nieh, Assessing the interfacial strength of an amorphous–crystalline interface. Acta Mater. **61**(9), 3304–3313 (2013)
16. L. Zhao, K.C. Chan, S.H. Chen, Atomistic deformation mechanisms of amorphous/polycrystalline metallic nanolaminates. Intermetallics **95**, 102–109 (2018)

17. S.D. Feng, L. Li, K.C. Chan, L. Qi, L. Zhao, L.M. Wang, R.P. Liu, Control of shear band dynamics in Cu50Zr50 metallic glass by introducing amorphous-crystalline interfaces. J. Alloy. Compd. **770**, 896–905 (2019)
18. W. Guo, E. Jägle, J. Yao, V. Maier, S. Korte-Kerzel, J.M. Schneider, D. Raabe, Intrinsic and extrinsic size effects in the deformation of amorphous CuZr/nanocrystalline Cu nanolaminates. Acta Mater. **80**, 94–106 (2014)
19. B. Arman, C. Brandl, S.N. Luo, T.C. Germann, A. Misra, T. Çağin, Plasticity in Cu (111)/Cu46Zr54 glass nanolaminates under uniaxial compression. J. Appl. Phys. **110**(4), 043539 (2011)
20. C.A. Schuh, T.C. Hufnagel, U. Ramamurty, Mechanical behavior of amorphous alloys. Acta Mater. **55**(12), 4067–4109 (2007)
21. Y.Q. Wang, J.Y. Zhang, X.Q. Liang, K. Wu, G. Liu, J. Sun, Size-and constituent-dependent deformation mechanisms and strain rate sensitivity in nanolaminated crystalline Cu/amorphous Cu–Zr films. Acta Mater. **95**, 132–144 (2015)
22. J.Y. Zhang, G. Liu, S.Y. Lei, J.J. Niu, J. Sun, Transition from homogeneous-like to shear-band deformation in nanolayered crystalline Cu/amorphous Cu–Zr micropillars: intrinsic vs. extrinsic size effect. Acta Mater. **60**(20), 7183–7196 (2012)
23. J.Y. Zhang, Y.Q. Wang, X.Q. Liang, F.L. Zeng, G. Liu, J. Sun, Size-dependent He-irradiated tolerance and plastic deformation of crystalline/amorphous Cu/Cu–Zr nanolaminates. Acta Mater. **92**, 140–151 (2015)
24. J.Y. Zhang, Y. Liu, J. Chen, Y. Chen, G. Liu, X. Zhang, J. Sun, Mechanical properties of crystalline Cu/Zr and crystal–amorphous Cu/Cu–Zr multilayers. Mater. Sci. Eng., A **552**, 392–398 (2012)
25. W.R. Jian, L. Wang, X.H. Yao, S.N. Luo, Tensile and nanoindentation deformation of amorphous/crystalline nanolaminates: effects of layer thickness and interface type. Comput. Mater. Sci. **154**, 225–233 (2018)
26. W.J. Lee, Y.C. Lo, A. Yang, K. Chen, N.Y. Chen, Thickness effect of nanocrystalline layer on the deformation mechanism of amorphous/crystalline multilayered structure. CMES **120**(2), 293–304 (2019)
27. C. Brandl, T.C. Germann, A. Misra, Structure and shear deformation of metallic crystalline–amorphous interfaces. Acta Mater. **61**(10), 3600–3611 (2013)
28. H. Zhou, S. Qu, W. Yang, An atomistic investigation of structural evolution in metallic glass matrix composites. Int. J. Plast **44**, 147–160 (2013)
29. J.Y. Zhang, G. Liu, J. Sun, Crystallization-aided extraordinary plastic deformation in nanolayered crystalline Cu/amorphous Cu-Zr micropillars. Sci. Rep. **3**(1), 1–6 (2013)
30. F. Abdeljaward, M. Haataja, Continuum modeling of bulk metallic glasses and composites. Phys. Rev. Lett. **105**, (2010)
31. G.P. Zheng, Application of phase-field modeling to deformation of metallic glasses. Curr. Opin. Solid State Mater. Sci. **15**, 116–124 (2011)
32. M.H. Lee, D.H. Bae, D.H. Kim, D.J. Sordelet, Synthesis of Ni-based bulk metallic glass matrix composites containing ductile brass phase by warm extrusion of gas atomized powders. J. Mater. Res. **18**(9), 2101–2108 (2003)
33. K. Durst, M. Göken, G.M. Pharr, Indentation size effect in spherical and pyramidal indentations. J. Phys. D Appl. Phys. **41**(7), (2008)
34. X.W. Zhou, R.A. Johnson, H.N.G. Wadley, Phys. Rev. B **69**, 144113 (2004)
35. M.I. Mendelev, M.J. Kramer, R.T. Ott, D.J. Sordelet, D. Yagodin, P. Popel, Development of suitable interatomic potentials for simulation of liquid and amorphous Cu–Zr alloys. Philos. Mag. **89**(11), 967–987 (2009)
36. M.I. Mendelev, D.J. Sordelet, M.J. Kramer, Using atomistic computer simulations to analyze x-ray diffraction data from metallic glasses. J. Appl. Phys. **102**(4), 043501 (2007)
37. M.I. Mendelev, M.J. Kramer, R.T. Ott, D.J. Sordelet, Molecular dynamics simulation of diffusion in supercooled Cu–Zr alloys. Philos. Mag. **89**(2), 109–126 (2009)
38. https://lammps.sandia.gov/
39. https://www.ovito.org/
40. C. Yang, C.T. Lo, A.F. Bastawros, B. Narasimhan, Measurements of diffusion thickness at polymer interfaces by nanoindentation: a numerically calibrated experimental approach. J. Mater. Res. **24**(3), 985–992 (2009)
41. D. Xu, B. Lohwongwatana, G. Duan, W.L. Johnson, C. Garland, Bulk metallic glass formation in binary Cu-rich alloy series–Cu100 – xZrx (x = 34, 36, 38.2, 40 at.%) and mechanical properties of bulk Cu64Zr36 glass. Acta Mater. **52**(9), 2621–2624 (2004)
42. Q. Guo, L. Zhang, A.S. Zeiger, Y. Li, K.J. Van Vliet, C.V. Thompson, Compositional dependence of Young's moduli for amorphous Cu–Zr films measured using combinatorial deposition on microscale cantilever arrays. Scr. Mater. **64**(1), 41–44 (2011)
43. J.C. Lee, K.W. Park, K.H. Kim, E. Fleury, B.J. Lee, M. Wakeda, Y. Shibutani, Origin of the plasticity in bulk amorphous alloys. J. Mater. Res. **22**(11), 3087–3097 (2007)
44. M.I. Mendelev, R.T. Ott, M. Heggen, M. Feuerebacher, M.J. Kramer, D.J. Sordelet, Deformation behavior of an amorphous Cu 64.5 Zr 35.5 alloy: a combined computer simulation and experimental study. J. Appl. Phys. **104**(12), 123532 (2008)
45. C. Deng, C.A. Schuh, Atomistic mechanisms of cyclic hardening in metallic glass. Appl. Phys. Lett. **100**(25), 251909 (2012)
46. C. Qiu, P. Zhu, F. Fang, D. Yuan, X. Shen, Study of nanoindentation behavior of amorphous alloy using molecular dynamics. Appl. Surf. Sci. **305**, 101–110 (2014)
47. T. Tsuru, Y. Shibutani, Anisotropic effects in elastic and incipient plastic deformation under (001), (110), and (111) nanoindentation of Al and Cu. Phys. Rev. B **75**(3), 035415 (2007)
48. H. Liang, C.H. Woo, H. Huang, A.H.W. Ngan, T.X. Yu, Crystalline plasticity on copper (001), (110), and (111) surfaces during nanoindentation. Comput. Model. Eng. Sci. **6**, 105–114 (2004)

49. K.L. Johnson, *Contact Mechanics* (Cambridge University Press, Cambridge, 1985)
50. A. Gouldstone, H.J. Koh, K.Y. Zeng, A.E. Giannakopoulos, S. Suresh, Discrete and continuous deformation during nanoindentation of thin films. Acta Mater. **48**(9), 2277–2295 (2000)
51. D.F. Bahr, D.E. Wilson, D.A. Crowson, Energy considerations regarding yield points during indentation. J. Mater. Res. **14**(6), 2269–2275 (1999)
52. W.C. Oliver, G.M. Pharr, An improved technique for determining hardness and elastic modulus using load and displacement sensing indentation experiments. J. Mater. Res. **7**(6), 1564–1583 (1992)
53. J.G. Swadener, E.P. George, G.M. Pharr, The correlation of the indentation size effect measured with indenters of various shapes. J. Mech. Phys. Solids **50**(4), 681–694 (2002)
54. G.Z. Voyiadjis, M. Yaghoobi, Large scale atomistic simulation of size effects during nanoindentation: dislocation length and hardness. Mater. Sci. Eng., A **634**, 20–31 (2015)
55. G. I. Taylor, The mechanism of plastic deformation of crystals. Part I.—Theoretical. Proceedings of the Royal Society of London. Series A, Containing Papers of a Mathematical and Physical Character **145**(855), 362–387 (1934)
56. W.D. Nix, H. Gao, Indentation size effects in crystalline materials: a law for strain gradient plasticity. J. Mech. Phys. Solids **46**(3), 411–425 (1998)
57. D.H. Bae, M.H. Lee, D.H. Kim, D.J. Sordelet, Plasticity in $Ni_{59}Zr_{20}Ti_{16}Si_2Sn_3$ metallic glass matrix composites containing brass fibers synthesized by warm extrusion of powders. Appl. Phys. Lett. **83**(12), 2312–2314 (2003)
58. H. Wang, A.F. Bastawros, S.B. Biner, Experimental observation of the failure mechanisms in a bulk metallic glass composite. Mater. Res. Soc. Symp. Proc. **1048**, 501 (2007)
59. L. Xiong, Y. Chen, Multiscale modeling and simulation of single-crystal MgO through an atomistic field theory. Int. J. Solids Struct. **46**(6), 1448–1455 (2009)
60. L. Xiong, A concurrent atomistic-continuum methodology and its applications, PhD Dissertation, Gainesville: University of Florida, (2011)
61. L. Xiong, Q. Deng, G. Tucker, D.L. McDowell, Y. Chen, A concurrent scheme for passing dislocations from atomistic to continuum domains. Acta Mater. **60**(3), 899–913 (2012)
62. S. Xu, L. Xiong, Y. Chen, D.L. McDowell, Sequential slip transfer of mixed-character dislocations across Σ3 coherent twin boundary in fcc metals: a concurrent atomistic-continuum study. NPJ Comput. Mater. **2**(1), 1–9 (2016)
63. S. Xu, L. Xiong, Q. Deng, D.L. McDowell, Mesh refinement scheme for the concurrent atomistic-continuum method. Int. J. Solids Struct. **90**, 144–152 (2016)
64. S. Xu, L. Xiong, Y. Chen, D.L. McDowell, Validation of the concurrent atomistic-continuum method on screw dislocation/stacking fault interactions. Crystals **7**(5), 120 (2017)
65. X. Chen, W. Li, L. Xiong, Y. Li, S. Yang, Z. Zheng, D.L. McDowell, Y. Chen, Ballistic-diffusive phonon heat transport across grain boundaries. Acta Mater. **136**, 355–365 (2017)
66. X. Chen, L. Xiong, D.L. McDowell, Y. Chen, Effects of phonons on mobility of dislocations and dislocation arrays. Scr. Mater. **137**, 22–26 (2017)
67. X. Chen, A. Diaz, L. Xiong, D.L. McDowell, Y. Chen, Passing waves from atomistic to continuum. J. Comput. Phys. **354**, 393–402 (2018)
68. S. Xu, T.G. Payne, H. Chen, Y. Liu, L. Xiong, Y. Chen, D.L. McDowell, PyCAC: the concurrent atomistic-continuum simulation environment. J. Mater. Res. **33**(7), 857 (2018)
69. H. Chen, S. Xu, W. Li, R. Ji, T. Phan, L. Xiong, A spatial decomposition parallel algorithm for a concurrent atomistic-continuum simulation and its preliminary applications. Comput. Mater. Sci. **144**, 1–10 (2018)